European Journal of Mechanics / A Solids 118 (2026) 106101

Contents lists available at ScienceDirect

European Journal of Mechanics / A Solids

journal homepage: www.elsevier.com/locate/ejmsol

Full Length Article

A physics-based crystal plasticity model for metallic material with highly pressurized bubbles

Quanfeng Han [a,b], Jingli Li [c], Hui Wang [a,b], Yizhe Chen [a,b,*], Xin Yi [d], Lin Hua [a,b,*]

[a] *State Key Laboratory of Light Superalloys, Wuhan University of Technology, Wuhan 430070, China*
[b] *School of Automotive Engineering, Wuhan University of Technology, Wuhan 430070, China*
[c] *Institute for Advanced Materials, North China Electric Power University, Beijing 102206, China*
[d] *School of Mechanics and Engineering Science, Peking University, Beijing 100871, China*

ARTICLE INFO

Keywords:
Hydrogen embrittlement
Hydrogen bubbles
Equation of state
Real behavior
Strength and ductility

ABSTRACT

Green hydrogen presents a promising route to a zero-emission future. However, hydrogen embrittlement may limit the potential of green hydrogen by weakening metallic structures, leading to leaks, cracks, and costly repairs. Acting as sites for crack initiation and local properties variation, hydrogen bubbles are considered to play an important role in hydrogen embrittlement by reducing the strength and ductility of metals. Existing theoretical models often rely on ideal gas assumptions, which do not account for the reduced compressibility of high-pressure hydrogen and lead to unrealistic estimation of metallic performance. This study presents a crystal plasticity model incorporating a Benedict-type equation of state for high-pressure hydrogen to accurately capture damage evolution in metals influenced by pressurized hydrogen bubbles. It is qualitatively revealed that ductility unexpectedly increases with the initial volume fraction and pressure of voids for polycrystalline copper, as increasing initial damage extent enhances strain-hardening capacity, distinct from the existing dislocation storage-based mechanism. This internal pressure applied to voids not only boosts macroscopic strain-hardening but also mitigates strain localization, delaying local necking and suggesting a promising pathway to improve the ductility of porous metals. Moreover, from a trend perspective, ideal gas models underestimate material strength and ductility due to compressibility differences. These qualitative insights contribute to the understanding in hydrogen embrittlement mechanisms and have implications for void swelling and helium embrittlement in irradiated metals.

1. Introduction

Green hydrogen, produced through water electrolysis powered by renewable electricity from solar and wind energy, stands out as a promising energy carrier for a climate-neutral society, significantly reducing the carbon footprint (Kourougianni et al., 2024; Niu et al., 2024; Liu et al., 2024). With an high energy density of 120 MJ/kg, —approximately three times that of kerosene (Prewitz et al., 2020; Yan et al., 2025)—hydrogen offers remarkable energy potential. Among the most critical issues in hydrogen storage and utilization is the hydrogen embrittlement of metallic materials, which presents a substantial risk to the safety and durability of hydrogen infrastructure (Huang et al., 2023; H. Zhao et al., 2024; Q. Zhao et al., 2024; Lopez-Cazalilla et al., 2024; Zhang et al., 2023; Magri, 2025).

In 1875, Johnson (1875) first documented the loss of strength, ductility, and fracture toughness in iron and steel exposed to acidic corrosion, attributing the deterioration to hydrogen penetration into the material. Since then, extensive research has sought to unravel the complex physical and chemical mechanisms behind hydrogen embrittlement in metals. Multiple hypotheses have emerged, including brittle hydride formation, hydrogen-enhanced decohesion, hydrogen-enhanced localized plasticity, dislocation ejection, hydrogen- and deformation-assisted vacancy generation, and high-pressure hydrogen bubbles (Robertson et al., 2015; Tan et al., 2024; Halilović et al., 2023). While no single theory fully accounts for the phenomenon, recent studies emphasize void formation as a key factor, as supported by mechanisms like hydrogen-enhanced localized plasticity, dislocation ejection, vacancy production, and the buildup of high hydrogen pressures within bubbles (Robertson et al., 2015; Y.-S. Chen et al., 2024).

Experimental studies and molecular dynamics simulations have consistently shown that hydrogen-assisted void nucleation and bubble growth frequently occur at phase interfaces and grain boundaries (Martinsson and Sandström, 2012; Chen et al., 2020; Peters et al., 2020; Xing et al., 2021, 2024; Xu et al., 2025). Additionally, solute hydrogen atoms can escape from trapping sites in the metallic matrix and

---

* Corresponding authors.
E-mail addresses: yzchen@whut.edu.cn (Y. Chen), hualin@whut.edu.cn (L. Hua).

https://doi.org/10.1016/j.euromechsol.2026.106101
Received 2 September 2025; Received in revised form 13 February 2026; Accepted 9 March 2026

then recombine to form hydrogen molecule at void surface (Ebling et al., 2025), and the thermodynamic equilibrium between the bulk lattice and void suggests that hydrogen bubble pressures can reach several gigapascals (Hou et al., 2019; Lopez-Cazalilla et al., 2022). Most importantly, the existing experimental studies demonstrated that the formation of highly pressurized hydrogen bubbles dominates the failure of copper shell used for spent nuclear fuel canisters (Sahiluoma et al., 2023; Martinsson and Sandström, 2012). Therefore, accurately modeling hydrogen embrittlement in metals requires careful consideration of hydrogen bubbles. Existing models have integrated voids, hydrogen diffusion in the matrix, and dislocation accumulation influenced by hydrogen content to predict embrittlement behavior (Yuan et al., 2023; Park et al., 2024; Pinto et al., 2024; Lindblom and Dahlberg, 2025). However, these approaches often overlook the effects of bubble pressure, which fluctuates with void volume during deformation. In general, both voids and their internal pressures accelerate material failure, even though dispersing nanovoids into pure gold indicates an exceptional enhancement of strength–ductility synergy in recent tensile experiments (J.-J. Chen et al., 2024). Therefore, neglecting bubble pressure can lead to unphysical predictions of residual strength and remaining service life of the metallic structures.

While some studies approximate the gas in voids as either ideal or constant-pressure gas (Guo et al., 2008; Yu et al., 2020; Das et al., 2021; Fu et al., 2024), this simplification may be inaccurate for hydrogen embrittlement. It is demonstrated that constant-pressure models predict lower flow stresses and faster void growth than ideal gas models (Guo et al., 2008). Additionally, real gases are generally less compressible, meaning they exhibit higher pressures than ideal gases of equal mass at given volumes and temperatures. Therefore, the macroscopic strength, ductility, and microstructural evolution in metals containing real-gas hydrogen bubbles are expected to deviate significantly from predictions based on ideal gas assumptions.

So far, no mechanistic model has coupled the real dynamic pressure evolution of hydrogen bubbles in porous metals, especially under extremely high internal pressures. In this study, for the first time we establish a crystal plasticity model that incorporates a Benedict-type equation of state, capturing void- and pressure-induced damage to qualitatively assess the impact of high-pressure hydrogen bubbles on material response (Section 2). Using copper as a test case, material parameters related to plastic slip and void damage are validated through homogenized porous single-crystal and representative volume element models (Section 3). The numerical simulations for polycrystalline copper indicate that the strength and ductility are significantly underestimated when assuming ideal gas behavior in high-pressure hydrogen voids (Section 4). Moreover, it is unexpectedly found that increasing bubble pressure is shown to enhance material ductility at mesoscale, validating the unusual trend previously observed only at the atomistic level through molecular dynamics simulation. Our studies further advance the understanding for hydrogen embrittlement and provide a more physical framework to assess the residual strength and service life of metallic materials and structures.

2. Crystal plasticity constitutive model for porous metals with high internal pressure

2.1. Equation of state (EOS) for hydrogen in voids

In prior studies on the failure behavior of porous metals with high internal pressure, the gas pressure inside voids is typically assumed constant or described by the ideal gas law (Guo et al., 2008; Yu et al., 2020; Das et al., 2021; Fu et al., 2024). However, *ab initio* calculations based on density functional theory demonstrate that the internal pressure of hydrogen bubbles can reach several gigapascals in metallic materials (Hou et al., 2019; Geng et al., 2017). Under such high pressures, hydrogen could transform to the supercritical fluid state (Wu and Li, 2025). Then the relationship among the internal pressure P, ambient temperature T, and molar volume V_{m} of the hydrogen in voids cannot be accurately described by the ideal gas equation $PV_{\mathrm{m}} = RT$, where R is the universal gas constant (8.314 J/(mol·K)). An EOS that accurately captures the behavior of hydrogen at high pressures is urgently needed.

Table 1

Dimensionless parameters of the Benedict-type EOS for real hydrogen (Matsuishi et al., 2002). Units for V_{m}, P, and T are cm^3/mole, 10^8 Pa, and K in Eq. (1), respectively.

n	$A_{n,1}$	$A_{n,2}$	$A_{n,3}$
−2	0	0	943.191
−1	89.5387	0	−307.938
0	31.964	−38.715	36.2153
1	0	0	0
2	−0.00935132	0.0680218	0.0105093

Based on experimentally measured sound velocities of fluid hydrogen, Matsuishi et al. (2002) formulated a Benedict-type EOS

$$V_{\mathrm{m}} = \sum_{m=1}^{3} \sum_{n=-2}^{2} A_{n,m} T^{n/2} P^{-m/3}, \tag{1}$$

where $A_{n,m}$ ($n = -2 \ldots 2$, $m = 1 \ldots 3$) are dimensionless fitted parameters (Table 1). Units for V_{m}, P, and T are cm^3/mole, 10^8 Pa, and K in Eq. (1), respectively. Within the wide range of $P \leq 15$ GPa and $T \leq 550$ K, Eq. (1) shows great accuracy in estimating both molar volume and sound velocity, showing an average deviation of only 1.0% from experimental results. Therefore, we employ Eq. (1) to characterize the evolution of pressure and density of highly pressurized hydrogen inside voids. For convenience, we will refer to hydrogen within voids as "ideal hydrogen" when it follows the ideal gas law and "real hydrogen" when it adheres to the Benedict-type EOS of Eq. (1). For real hydrogen, the critical temperature, above which gas cannot be liquefied, is $T_{\mathrm{c}} = 33.3$ K, and there exists no distinguishable phase boundary between gas and fluid (Hemmes et al., 1986). In contrast, the fluid–solid phase boundary can be uniquely determined by the modified Simon melting equation $P_{\mathrm{m}} = -0.5149 + 1.702 \times 10^{-3}(T_{\mathrm{m}} + 9.689)^{1.8077}$ with T_{m} (K) and P_{m} (10^8 Pa) as melting temperature and melting pressure, respectively (Diatschenko et al., 1985). To avoid the problem of gas–liquid separation in the numerical simulation, only the melting line above $T = 100$ K is present in Fig. 1a. At $T = 300$ K and $P < 5.366$ GPa, hydrogen remains in a supercritical fluid state accordingly. Fig. 1b presents the compressibility factor, $Z = PV_{\mathrm{m}}/(RT)$, of hydrogen under the different laws. For the real hydrogen depicted by Eq. (1), Z increases rapidly from its initial value of one as the pressure P rises at a given temperature T, suggesting an enhancement in incompressibility with increasing pressure. Conversely, Z decreases as temperature T increases at a fixed internal pressure. For ideal hydrogen, however, Z remains constant at one, regardless of P or T.

2.2. Constitutive model for plastic slip in grains containing voids

For grains containing voids, the plastic deformation rate tensor $\mathbf{D}_{\mathrm{p}}$ is expressed as (Han et al., 2013)

$$\mathbf{D}_{\mathrm{p}} = \frac{1 - f_{\mathrm{v}}}{2} \sum_{i=1}^{N_{\mathrm{s}}} \dot{\gamma}_i \left[\mathbf{N}_i^{\mathrm{eff}} + \left(\mathbf{N}_i^{\mathrm{eff}}\right)^{\mathrm{T}} \right], \tag{2}$$

where f_{v} is the volume fraction of voids, $\dot{\gamma}_i$ is the microscopic plastic slip rate of dislocation associated with the i-th slip system, $\mathbf{N}_i^{\mathrm{eff}}$ is the effective Schmid tensor determined by the internal pressure-dependent Gurson–Tvergaard–Needleman (GTN) potential function of porous single crystal (detailed in Section 2.3), and the superscript T represents the transpose. Experimental studies suggested that in the copper shell of spent nuclear fuel canisters, the formation of numerous hydrogen bubbles near the surface is the primary driver of hydrogen embrittlement (Sahiluoma et al., 2023). Furthermore, previous research

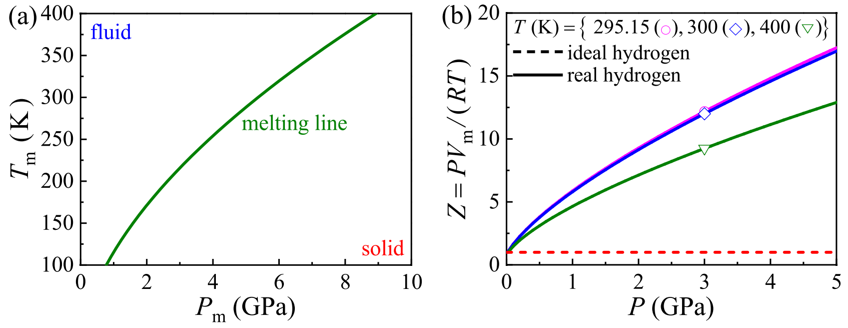

Fig. 1. (a) Melting temperature T_m as function of melting pressure P_m for hydrogen. (b) Compressibility coefficient $Z = PV_\mathrm{m}/(RT)$ versus internal pressure P for ideal and real hydrogen at different values of temperature T. Units for P_m, P, and T_m are GPa, GPa, and K in the figure, respectively.

indicated that hydride formation in copper is unlikely at pressures below 5 GPa (Condon and Schober, 1993). Therefore, other hydrogen-induced mechanisms are expected to play a less significant role and can reasonably be omitted when considering the hydrogen embrittlement of copper in this context. Based on these two aspects, the coarse-grained copper is selected as a representative to solely investigate the influence of EOS on the macroscopic mechanical response and microstructural evolution of metallic materials. Correspondingly, there are $N_\mathrm{s} = 12$ slip systems for the face-centered cubic metals.

In general, $\dot{\gamma}_i$ is described by the following phenomenological law (Hutchinson, 1976; Hu et al., 2024; Chen et al., 2025)

$$\dot{\gamma}_i = \dot{\gamma}^0 \left| \frac{\tau_i^\mathrm{eff}}{\tau_i^\mathrm{c}} \right|^{1/m} \mathrm{sgn}(\tau_i^\mathrm{eff}), \tag{3}$$

where $\dot{\gamma}^0$, m, and τ_i^c denote the referenced shear strain rate, strain rate sensitivity parameter, and critical resolved shear stress of the i-th slip system, respectively. As the grain size effect is negligible for coarse-grained metals, and Orowan strengthening from dispersed voids is not considered here, τ_i^c is depicted by the Taylor-strengthening law $\tau_i^\mathrm{c} = \alpha\mu b\sqrt{\rho_i}$, neglecting the experimentally observed strengthening effect due to dispersed nanovoids in materials (J.-J. Chen et al., 2024), where α, μ, b, and ρ_i represent a dimensionless constant, the shear modulus, the Burgers vector length of a full dislocation, and the dislocation density in the i-th slip system, respectively. Due to the presence of voids in the grains, the effective resolved shear stress τ_i^eff is determined by the internal pressure-dependent GTN potential function, as discussed in Section 2.3.

During the plastic deformation, the dislocations within grains multiply and annihilate due to interactions among themselves and pile-ups at grain boundaries. The dynamic evolution rate $\dot{\rho}_i$ of the dislocation density is described by

$$\dot{\rho}_i = \frac{1}{b}\left(\frac{\sqrt{\rho_i}}{K} - 2y_\mathrm{c}\rho_i \right) \left| \dot{\gamma}_i \right|, \tag{4}$$

where K is a dimensionless constant governing dislocation propagation for coarse-grained copper, and y_c denotes the critical annihilation distance between two attractive edge dislocations. From Eq. (4), the saturated dislocation density is determined for each slip system within the grains as $\rho_i^\mathrm{sat} = 1/(2Ky_\mathrm{c})^2$.

2.3. Internal pressure-dependent damage model for grains containing voids

Both the presences of voids within a grain and their internal pressure significantly degrade the mechanical performance of metallic materials. Leveraging a variational approach, Yu et al. (2020) develop the following internal pressure-dependent GTN potential function for a homogenized porous single crystal

$$\begin{aligned} \Psi = {} & \left(\frac{\tau_i}{\tau_i^\mathrm{eff}} \right)^2 + \frac{2 f_\mathrm{v}^\mathrm{eff} P \tau_i}{(\tau_i^\mathrm{eff})^2} + \frac{2}{45}\lambda f_\mathrm{v}^\mathrm{eff} \left(\frac{\sigma^\mathrm{eq}}{\tau_i^\mathrm{eff}} \right)^2 \\ & + 2q_1 f_\mathrm{v}^\mathrm{eff} \cosh\left[q_2 \sqrt{ \frac{3}{10} \frac{P\sigma^\mathrm{m}}{(\tau_i^\mathrm{eff})^2} + \frac{3}{20} \left(\frac{\sigma^\mathrm{m}}{\tau_i^\mathrm{eff}} \right)^2 } \right] - 1 - (q_1 f_\mathrm{v}^\mathrm{eff})^2 = 0 \end{aligned}, \tag{5}$$

where the resolved shear stress τ_i is defined as $\tau_i = \boldsymbol{\sigma} : (\mathbf{m}_i \otimes \mathbf{n}_i)$, with $\boldsymbol{\sigma}$ as the Cauchy stress tensor, and $\mathbf{n}_i$ and $\mathbf{m}_i$ represent the unit vectors defining the normal and slip directions for the i-th slip system in the dense matrix, respectively. σ^eq and σ^m denote the von Mises equivalent stress and hydrostatic stress derived by the Cauchy stress tensor $\boldsymbol{\sigma}$, respectively. Parameters λ, q_1, and q_2 are adjustable dimensionless constants. In Eq. (5), the terms associated with $f_\mathrm{v}^\mathrm{eff}$ and P indicate the enhancing effect of voids and internal pressure on dislocation motion. Since both voids and their internal pressure induce damage, the effective resolved shear stress $\tau_\mathrm{i}^\mathrm{eff}$ acting on the i-th slip system increases, as defined in Eq. (5). According to Eq. (3), this leads to an elevated microscopic plastic slip rate $\dot{\gamma}_i$, which in turn accelerates dislocation accumulation through Eq. (4), given that dislocation multiplication is directly proportional to $\dot{\gamma}_i$. Additionally, the term associated with σ^m reflects the contribution of hydrostatic stress to void growth. For variable internal pressure P, detailed solving procedures for real and ideal hydrogen are outlined in the Appendix A. Assuming no void nucleation within the grain, with incompressible dense matrix and neglecting void coalescence effects, the effective void fraction $f_\mathrm{v}^\mathrm{eff}$ is described by the following piecewise function

$$f_\mathrm{v}^\mathrm{eff} = \begin{cases} f_\mathrm{v}, & f_\mathrm{v} \le 1/q_1, \\ 1/q_1, & f_\mathrm{v} > 1/q_1, \end{cases} \tag{6}$$

where f_v is the void volume fraction and its growth rate is

$$\dot{f}_\mathrm{v} = (1 - f_\mathrm{v})\mathrm{trace}(\mathbf{D}_\mathrm{p}). \tag{7}$$

Using Eq. (5), the value of τ_i^eff can be calculated iteratively, with its sign matching that of τ_i. In general, this scalar is objective under the continuum mechanics framework. However, we find that the absolute value of τ_i^eff determined by Eq. (5) varies depending on the sign of τ_i, which conflicts with the objectivity principle. To ensure full compliance with this principle, Eq. (5) is revised as

$$\begin{aligned} \Psi = {} & \left(\frac{\tau_i}{\tau_i^\mathrm{eff}} \right)^2 + \frac{2 f_\mathrm{v}^\mathrm{eff} P |\tau_i|}{(\tau_i^\mathrm{eff})^2} + \frac{2}{45}\lambda f_\mathrm{v}^\mathrm{eff} \left(\frac{\sigma^\mathrm{eq}}{\tau_i^\mathrm{eff}} \right)^2 \\ & + 2q_1 f_\mathrm{v}^\mathrm{eff} \cosh\left[q_2 \sqrt{ \frac{3}{10} \frac{P\sigma^\mathrm{m}}{(\tau_i^\mathrm{eff})^2} + \frac{3}{20} \left(\frac{\sigma^\mathrm{m}}{\tau_i^\mathrm{eff}} \right)^2 } \right] - 1 - \left(q_1 f_\mathrm{v}^\mathrm{eff}\right)^2 = 0 \end{aligned}. \tag{8}$$

Using Eq. (8), the normality rule in elastic–plastic mechanics, and the implicit function theorem, the effective Schmid tensor is given by

$$\mathbf{N}_i^{\mathrm{eff}} = \frac{\partial \tau_i^{\mathrm{eff}}}{\partial \boldsymbol{\sigma}} = -\frac{\partial \Psi / \partial \boldsymbol{\sigma}}{\partial \Psi / \partial \tau_i^{\mathrm{eff}}}, \tag{9}$$

where

$$\begin{aligned} \frac{\partial \Psi}{\partial \boldsymbol{\sigma}} = {} & \frac{2\tau_i}{(\tau_i^{\mathrm{eff}})^2}\mathbf{N}_i + \frac{2 f_{\mathrm{v}}^{\mathrm{eff}} P \operatorname{sgn}(\tau_i)}{(\tau_i^{\mathrm{eff}})^2}\mathbf{N}_i + \frac{2}{15}\frac{\lambda f_{\mathrm{v}}^{\mathrm{eff}}}{(\tau_i^{\mathrm{eff}})^2}\mathbf{S} \\ & + \frac{q_1 q_2 f_{\mathrm{v}}^{\mathrm{eff}}}{10\sqrt{\frac{3}{10}\frac{P\sigma^{\mathrm{m}}}{(\tau_i^{\mathrm{eff}})^2} + \frac{3}{20}\left(\frac{\sigma^{\mathrm{m}}}{\tau_i^{\mathrm{eff}}}\right)^2}} \\ & \times \sinh\left[q_2\sqrt{\frac{3}{10}\frac{P\sigma^{\mathrm{m}}}{(\tau_i^{\mathrm{eff}})^2} + \frac{3}{20}\left(\frac{\sigma^{\mathrm{m}}}{\tau_i^{\mathrm{eff}}}\right)^2}\right] \times \left[\frac{P}{(\tau_i^{\mathrm{eff}})^2} + \frac{\sigma^{\mathrm{m}}}{(\tau_i^{\mathrm{eff}})^2}\right]\mathbf{I} \end{aligned},$$

$$\begin{aligned} \frac{\partial \Psi}{\partial \tau_i^{\mathrm{eff}}} = {} & -\frac{2}{\tau_i^{\mathrm{eff}}}\left(\frac{\tau_i}{\tau_i^{\mathrm{eff}}}\right)^2 - \frac{4 f_{\mathrm{v}}^{\mathrm{eff}} P \left|\tau_i\right|}{(\tau_i^{\mathrm{eff}})^3} - \frac{4}{45}\frac{\lambda f_{\mathrm{v}}^{\mathrm{eff}}}{\tau_i^{\mathrm{eff}}}\left(\frac{\sigma^{\mathrm{eq}}}{\tau_i^{\mathrm{eff}}}\right)^2 \\ & - \frac{2 q_1 q_2 f_{\mathrm{v}}^{\mathrm{eff}}}{\tau_i^{\mathrm{eff}}} \times \sinh\left[q_2\sqrt{\frac{3}{10}\frac{P\sigma^{\mathrm{m}}}{(\tau_i^{\mathrm{eff}})^2} + \frac{3}{20}\left(\frac{\sigma^{\mathrm{m}}}{\tau_i^{\mathrm{eff}}}\right)^2}\right], \\ & \times \sqrt{\frac{3}{10}\frac{P\sigma^{\mathrm{m}}}{(\tau_i^{\mathrm{eff}})^2} + \frac{3}{20}\left(\frac{\sigma^{\mathrm{m}}}{\tau_i^{\mathrm{eff}}}\right)^2} \end{aligned}$$

with $\mathbf{N}_i = \mathbf{m}_i \otimes \mathbf{n}_i$ as the Schmid tensor, $\mathbf{S} = \boldsymbol{\sigma} - \sigma^{\mathrm{m}}\mathbf{I}$ as the deviatoric stress tensor, and $\mathbf{I}$ as the second-order identity tensor. Specially, at $P = 0$ GPa, Eq. (8) degenerates to the potential function for the metallic materials without pressurized gas inside voids proposed by Han et al. (2013). Furthermore, at $f_{\mathrm{v}} = 0$, Eq. (8) reduces to the case for a dense matrix material without void.

Up to this point, a crystal plasticity constitutive model has been established that couples the evolution of internal pressure of hydrogen obeying different laws with internal pressure-dependent void damage. This constitutive model can be implemented in ABAQUS software using the UMAT and UVARM subroutines, as illustrated in the flowchart in Fig. 2. In the present work, the implicit integration method is adopted to solve the relevant differential equations, including Eqs. (3), (4) and so on. Hereinafter, C3D8R element is adopted in the finite element simulation.

For metallic materials subjected to neutron irradiation, the formation of high-pressure helium bubbles has been experimentally observed (Miura et al., 2015). By using the fitted parameters $A_{n,m}$ for high-pressure helium (Mills et al., 1980) in Eq. (A.3) in the Appendix A, the dynamic evolution of pressure in the helium bubbles can be described. Therefore, the proposed theoretical framework can be readily extended to investigate void swelling and helium embrittlement in irradiated metallic materials. In addition, though the face-centered cubic copper is chosen as an example in this work, the established framework is also applicable to both the body-centered cubic and hexagonal close-packed metals.

3. Validation of material parameters for dense matrix and void damage in single-crystal copper

3.1. Material parameters for the dense matrix

To examine the internal pressure-dependent mechanical behavior of polycrystalline copper, the material parameters for single-crystal copper (without voids) are first established. Table 2 presents the material parameters relevant to the plastic slip and dislocation evolution in dense single-crystal copper for use in numerical simulations. In Table 2, the shear modulus μ of the dense matrix at $T = 295.15$K is estimated using the Voigt–Reuss–Hill average (Hill, 1952)

$$\mu = \frac{1}{2}\left[\frac{1}{5}(C_{11} - C_{12} + 3C_{44}) + \frac{5(C_{11} - C_{12})C_{44}}{3(C_{11} - C_{12}) + 4C_{44}}\right], \tag{10}$$

where the temperature-dependent elastic constants C_{ij} are defined as $C_{ij}(T) = C_{ij}^0 - S_{ij}/[\exp(T_{ij}/T) - 1]$ ($i = 1, 4$ and $j = 1, 2, 4$). Table 3 lists the elastic constants C_{ij}^0 at $T = 0$ K alongside the fitted parameters S_{ij} and T_{ij} from experimental data below 300 K (Varshni, 1970). Here, the subscripts i and j obey Voigt notation. As these elastic parameters are strictly valid at temperature below 300 K, the viscoplastic flow of copper, which is described by Eqs. (2), (3), (8), (9) and so on, is physically accurate at $T < 300$ K.

Fig. 3 compares the simulated strain–stress curves with experimental results for uniaxial tension of single-crystal copper at a nominal strain rate $\dot{\varepsilon}_{11}^{\mathrm{nom}} = 10^{-4}$/s, under the ambient temperature $T = 295.15$ K (Takeuchi, 1975). For the cases of [100] and [111] loadings, the close agreement between numerical and experimental tensile stress–strain curves supports the validity of the constitutive model presented in Section 2, as well as the material parameters listed in Tables 2 and 3. Additionally, the special coplanar double slip of dislocation reduces the strain hardening rate of material at [101] loading (Zepeda-Ruiz et al., 2021). As we employ a common hardening model neglecting this mechanism, there will exist discrepancy between the predicted stress–strain curve and experimental result at [101] loading when using existing material parameters calibrated by the [111] and [100] loadings. However, it offers a valuable direction for addressing orientation-specific behavior. The coplanar double slip is a critical mechanism to be incorporated into the existing constitutive model in future work. In fact, for polycrystalline metallic materials, as all grain orientations are randomly assigned and these grains undergo a complex multiaxial stress, few grains deform plastically through the coplanar double slip mechanism. One can expect that the absence of coplanar double slip mechanism has little influence on the macroscopic stress–strain response of polycrystalline metallic materials in the following sections. In the following finite element simulations, all samples are subjected to uniaxial loading along x-axis at $\dot{\varepsilon}_{11}^{\mathrm{nom}} = 10^{-4}$/s and $T = 295.15$ K.

3.2. Material parameters for void damage

Fitting the yield strength of unit cell models with differing crystallographic orientations, Han et al. (2013) determined optimized values for the dimensionless parameters λ, q_1, and q_2, as shown in Table 4, for porous metals without internal pressure. Using the unit cell model of single-crystal copper with an embedded void (Fig. 4) as an example, we examine the applicability of these parameters in describing the plastic behavior of porous metals with internal pressure.

In the unit cell model (Fig. 4), the dense matrix is assumed incompressible by setting $f_{\mathrm{v}} = 0$ in Eq. (8). Void volume and the pressure and density of the internal hydrogen are variable. Here, the hydrogen bubble is modeled as a fluid cavity, and the constitutive behavior of hydrogen, governed by either the ideal gas law of $PV_{\mathrm{m}} = RT$ or the Benedict-type EOS of Eq. (1), is incorporated via the UFLUID subroutine in ABAQUS. The finite element simulation for the unit cell model proceeds as follows: at the outset, periodic boundary conditions detailed in Section 4.1 are applied in x, y, and z directions, with matrix material parameters consistent with those of single-crystal copper as defined in Section 3.1. In the initial loading step, the fluid cavity pressure increases from 0 MPa to 700 MPa. The unit cell model then undergoes uniaxial tensile loading along x-axis in the second loading step. In the loading process, both the temperatures of dense matrix and fluid cavity are considered as a constant of $T = 295.15$ K. For the unit cell model, the void volume fraction is calculated as $f_{\mathrm{v}} = V_{\mathrm{cav}}/(V_{\mathrm{cav}} + V_{\mathrm{mat}})$, where V_{cav} and V_{mat} represent the volumes of the fluid cavity and the dense matrix, respectively. The post-processor of the ABAQUS software is utilized to extract V_{cav}.

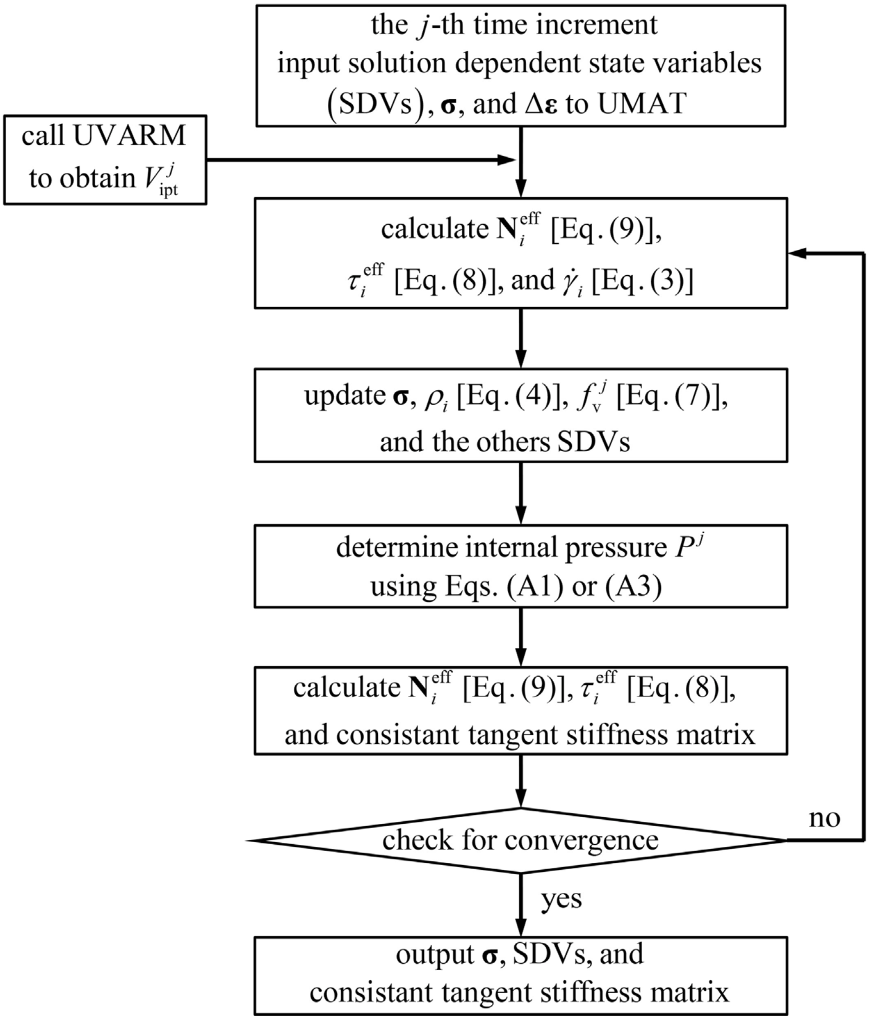

Fig. 2. Flowchart illustrating the implementation of the UMAT, which incorporates the evolution of internal pressure of hydrogen within voids. The superscript j here is used to identify quantities immediately following the j-th time increment. The iteration is considered convergent when the relative error of each $\dot{\gamma}_i$ between two successive iterative steps falls below 10^{-4}.

Table 2
Material parameters for plastic slip and dislocation evolution of single crystal copper.

Parameters	Definition	Values	References
K	Dimensionless constant	12.1	Fitted parameter
b	Burgers vector length	0.256 nm	Xiao et al. (2015)
$1/m$	Strain rate sensitivity parameter	30	Fitted parameter
y_c	Critical annihilation distance	4.23 nm	Walgraef and Ghoniem (1990)
α	Dimensionless constant	1	Xiao et al. (2015)
$\dot{\gamma}^0$	Referenced shear strain rate	10^{-4}/s	Xiao et al. (2015)
μ	Shear modulus	47.43 GPa	Voigt–Reuss–Hill average
ρ_i^0	Initial dislocation density	$1.4\times10^{11}/\mathrm{m}^2$	Fitted parameter

Table 3
Temperature-dependent elastic constants for dense single-crystal copper (Varshni, 1970).

Elastic constants	C_{ij}^0 (MPa)	S_{ij} (MPa)	T_{ij} (K)
C_{11}	176 094	7600.4	206.4
C_{12}	124 892	2383.6	158.4
C_{44}	81 706	4528.3	163.4

For the homogenized porous single crystal, referred to as the internal pressure-dependent GTN model hereinafter, the material parameters in Tables 2 to 4 are employed, with the exception of the initiation dislocation density ρ_i^0 associated with the i-th slip system and the initial volume fraction f_{v}^0 of voids. Corresponding values of initial void volume fraction and initial dislocation density are determined by $f_{\mathrm{v}} = V_{\mathrm{cav}}/(V_{\mathrm{cav}}+V_{\mathrm{mat}})$ and $\rho_i^0 = \sum_{k=1}^{N_{\mathrm{ipt}}} \rho_k^{\mathrm{tol}} V_{\mathrm{ipt},k}/12(V_{\mathrm{cav}}+V_{\mathrm{mat}})$ of the unit cell model at the end of aforementioned first loading step, respectively, where ρ_k^{tol} and $V_{\mathrm{ipt},k}$ are the total intragranular dislocation density and volume associated with the k-th integration point, respectively. N_{ipt} is the total number of integration points in the computational domain. In ABAQUS software, the integration volume at each Gauss point, which is obtained through UVARM subroutine as shown in Fig. 2, is defined as the product of its weight coefficient and the corresponding Jacobian determinant of element. Hereinafter other macroscopic variables, including the strain component ε_{11} and stress component σ_{11} along x-direction, total intragranular dislocation density ρ^{tol}, average grain

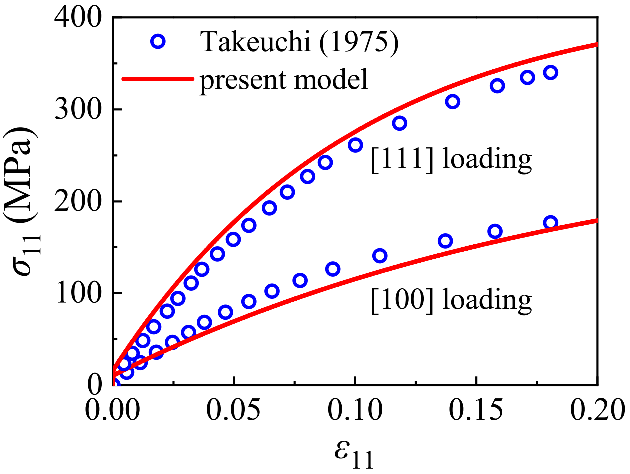

Fig. 3. Comparison of true stress–strain curves from numerical simulations and experimental results (Takeuchi, 1975) for uniaxial tension of single-crystal copper at $T = 295.15$ K.

Table 4
Material parameters for void damage (Han et al., 2013).

Parameters	λ	q_1	q_2
Values	6.456	1.471	1.325

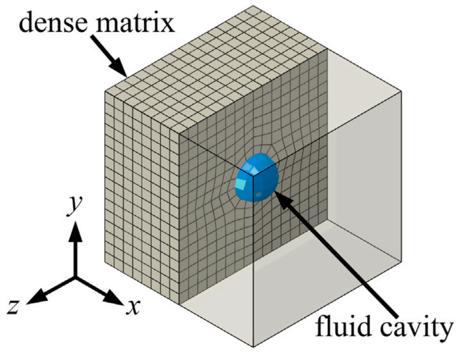

Fig. 4. Unit cell model of a single crystal containing voids. The matrix is dense by setting initial void volume fraction $f_v = 0$, and the void in material is modeled by fluid cavity.

diameter $d_{\rm ave}$ and so on, are also determined using the volume-weighted method. For example, the macroscopic tensile flow stress of sample under uniaxial loading is $\sigma_{11} = \sum_{k=1}^{N_{\rm ipt}} \sigma_{11,k} V_{{\rm ipt},k} / \sum_{k=1}^{N_{\rm ipt}} V_{{\rm ipt},k}$ as defined in our previous work (Han et al., 2023), where $\sigma_{11,k}$ is the stress component along x-direction of the k-th integration point.

Fig. 5 shows the volume-weighted true stress–strain curves for both the internal pressure-dependent GTN model and the unit cell model with the real and ideal hydrogen. The flow stresses at a 0.2% offset strain for both models are nearly identical for samples subjected to a given loading direction. This observation indicates that the dimensionless parameters for void damage listed in Table 4 accurately capture the initial yield behavior of the homogenized porous single crystal with internal pressure. However, the discrepancy between the unit cell and internal pressure-dependent GTN models becomes more pronounced with increasing strain for both samples. This discrepancy can be attributed to the differing rates of void growth in the two models. In general, the growth rate of void volume fraction is quite slow at small strain for the conventional internal pressure-independent GTN model. Numerical results in Fig. 6 indicate that the void volume fraction f_v in the internal pressure-dependent GTN model increases more significantly than in the unit cell model as strain increases at $P^0 = 700$ MPa, suggesting the dominant role of internal pressure in accelerating void growth in the internal pressure-dependent GTN model at small strain. Low stress triaxiality is the main reason for the extremely small growth rate of voids in the unit cell model. Under uniaxial tensile loading, voids elongate, which further slows their growth. Although the internal pressure in the voids decreases with increasing void volume fraction, the extent of damage in the internal pressure-dependent GTN model is considerably more severe than in the unit cell model due to the larger void volume fraction, leading to a substantial reduction in the macroscopic flow stress of the internal pressure-dependent GTN model. However, both the stress–strain curves and evolution curves of void volume fraction are nearly identical for these two models at $P = 0$ MPa under different loading direction as shown in Fig. 7. Above results suggests that internal pressure more significantly accelerates void growth in the internal pressure-dependent GTN model than the unit cell model in post-yield stage.

Building on the pioneering theoretical work of Gurson (1977) on the yield behavior of porous metals, Han et al. (2013) introduced additional parameters λ, q_1, and q_2 in Eq. (8) with $P = 0$ GPa to improve the model's accuracy. In this work, one can see the marked disparity between the internal pressure-dependent GTN and unit cell models (Fig. 5). Meanwhile, molecular dynamics simulations of uniaxial tension in nano-twinned copper demonstrated that internal pressure significantly accelerates the growth of helium bubbles at a certain macroscopic strain rate (Sun et al., 2019), in line with the trends observed in the internal pressure-dependent GTN model. Therefore, combining these two aspects, quantitatively refining the dimensionless parameters λ, q_1, and q_2 in Eq. (8) are required to reduce the divergence in post yield stage between the internal pressure-dependent GTN model and unit cell model, through the simulations at different internal pressures and crystal orientations following the approach of Han et al. (2013). However, due to the high computational cost and time cost, this refinement falls outside the scope of the present work and could be investigated in detail in future work. The dimensionless parameters in Table 4 are retained to qualitatively explore the macroscopic damage behavior and microstructural evolution of polycrystalline copper in Section 4.

4. Macroscopic mechanical response and microstructural evolution of polycrystalline copper

The quantitative measurement for the internal pressure within the hydrogen bubble of metallic material remains challenging in the experimental study. This section will numerically and qualitatively investigate the influences of EOS choice and internal pressure on the estimation of macroscopic properties and the microstructural evolutions of materials, including yield strength, fracture strength, uniform tensile strain, internal pressure variation, dislocation multiplication, and necking formation.

4.1. EOS-dependent mechanical behavior

Fig. 8 shows the untextured polycrystalline internal pressure-dependent GTN sample, with edge length $L = 120$ μm and containing $N_G = 150$ equiaxed grains of average grain diameter $d_{\rm ave} = 29.5$ μm, used to investigate the macroscopic mechanical response and microstructural evolution of coarse-grained copper. The element length is set at 5 μm by evaluating the convergence of numerical results and the computational efficiency as detailed in Appendix B. In general, as single crystals exhibit anisotropic mechanical behavior at the microscopic scale, a material comprising a limited number of grains displays direction-dependent flow stresses at the macroscopic scale. According to the criterion proposed by Nygårds (2003), if the material behavior is purely elastic, the estimated error in macroscopic flow stress due to microscopic heterogeneity is approximately 2.1% for

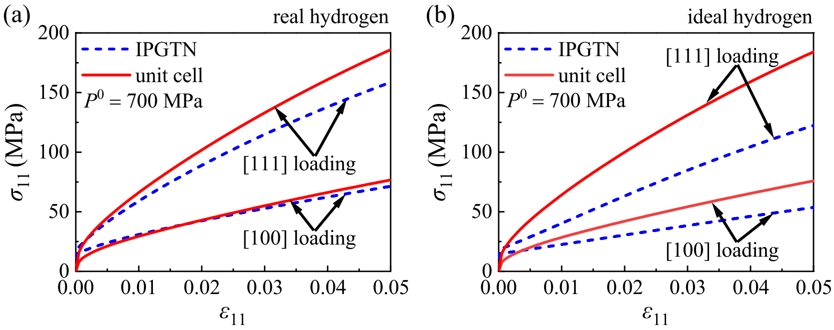

Fig. 5. True stress–strain curves for the internal pressure-dependent GTN (IPGTN) and unit cell models with the real (a) and ideal (b) hydrogen in the voids, each at an initial internal pressure $P^0 = 700$ MPa.

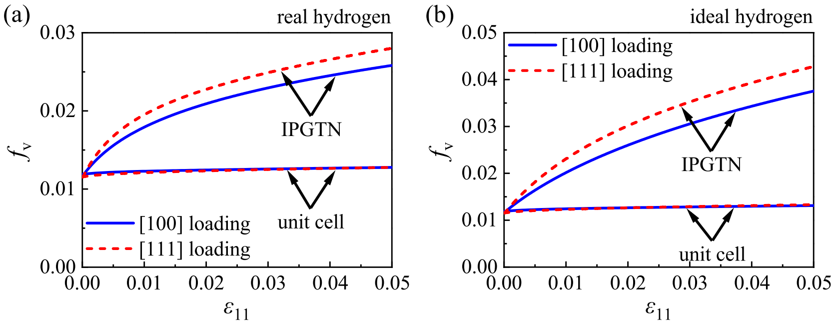

Fig. 6. Void volume fraction f_v as a function of uniaxial tensile strain ε_{11} in the internal pressure-dependent GTN and unit cell models with the real (a) and ideal (b) hydrogen in the voids.

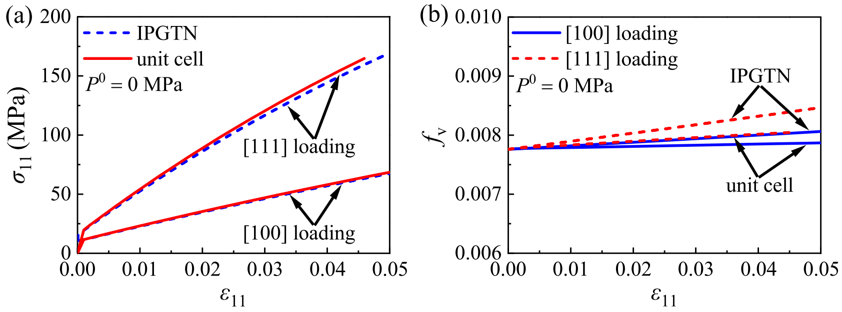

Fig. 7. True stress–strain curves (a) and void volume fraction f_v as a function of uniaxial tensile strain ε_{11} (b) for the internal pressure-dependent GTN (IPGTN) and unit cell models at $P = 0$ MPa.

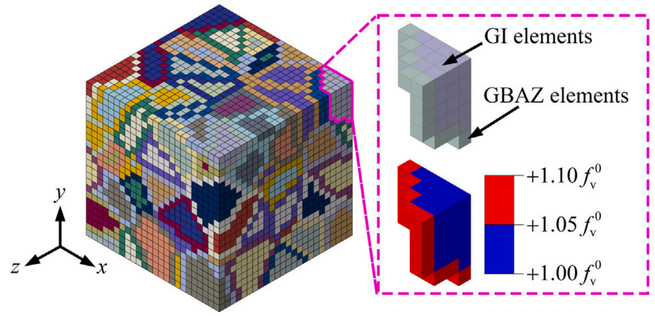

Fig. 8. Polycrystalline model with randomly distributed equiaxed grains. GI, grain interior; GBAZ, grain boundary affected zone.

the polycrystalline model in Fig. 8. However, the plastic response of polycrystalline metallic materials is inherently more complex than their elastic response. Therefore, to assess the isotropy and reliability of our model under plastic deformation, we conducted additional simulations under various loading directions, as detailed in Appendix B. The results presented in Fig. B.2 demonstrate that the polycrystalline model in Fig. 8 exhibits isotropic elastic–plastic behavior, indicating that the numerical results presented in this study are sufficiently accurate for the intended analyses. Due to random crystallographic orientations, the microscopic heterogeneity of single crystals within a polycrystalline material can lead to localized stress concentration. As a result, strain localization and necking can develop in the sample under uniaxial tensile loading. To exclude the potential influence of localized necking on the macroscopic mechanical response, the periodic boundary conditions described by $\mathbf{u}^{r+} - \mathbf{u}^{r-} = \mathbf{U}^s - \mathbf{U}^0$ $(r, s = x, y, z)$ (Kim et al., 2017) are applied across all three spatial dimensions for the

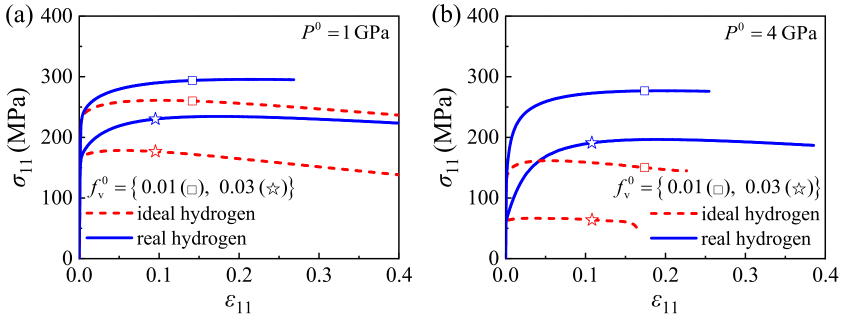

Fig. 9. True stress–strain curves for polycrystalline samples with the ideal and real hydrogen in voids at $P^0 = 1$ GPa (a) and 4 GPa (b).

nodes at boundary surfaces to ensure uniform deformation at large strains, where $\mathbf{u}$ and $\mathbf{U}$ are the displacement vectors of boundary surface node and master node, respectively, superscripts $r+$ and $r-$ denote the corresponding nodes on opposite boundary surfaces, and $\mathbf{U}^0$ is the displacement vector of node at origin. In general, the periodic microstructure is preferred due to the limitation in mesh conformity for periodic boundary condition. As the voxelization-based model satisfies this restriction voluntarily, the periodic boundary condition remains appropriate to obtain the homogenized response for the non-periodic model in Fig. 8.

For metallic materials, the grain boundaries serve as preferential sites for hydrogen atom trapping, promoting nucleation and concentration of hydrogen bubbles near these regions (Chen et al., 2020; Peters et al., 2020; Xing et al., 2021). It has been experimentally observed that hydrogen bubbles are prone to form at grain boundaries and triple junctions in the aforementioned copper used for spent nuclear fuel canisters (Martinsson and Sandström, 2012). Here, the initial void volume fractions are qualitatively taken as f_v^0 and $1.1f_v^0$ for the elements in the grain interiors and grain boundary affected zones, respectively, to incorporate hydrogen-induced boundary weakening, which serves as a simplified representation of the variation in hydrogen concentration between these two regions. The existing numerical study for the helium embrittlement of metallic materials has adopted a similar structure-dependent spatial distribution, despite larger ratio of void volume fraction between grain interior and grain boundary affected zone (Fu et al., 2024). While the current model focuses on the mechanical effects of internal pressure from hydrogen bubbles, it does not explicitly incorporate other known embrittlement mechanisms, such as hydrogen-induced reduction in grain boundary cohesion or dislocation–boundary interactions. These aspects will be considered in future model developments. In addition, the internal pressure inside voids can induce severe plastic deformation even before external loading, significantly increasing the initial dislocation density in the material. Therefore, the initial dislocation density belonging to the i-th slip system is set at $\rho_i^0 = 0.8\rho_i^{\text{sat}}$ where the initial total dislocation density is set to a value comparable to that observed in materials subjected to extensive cold deformation. With setting different initial values for P in Eq. (8) at the beginning of numerical simulation, the pressure inside voids is imposed into the polycrystalline model in Fig. 8. As analyzed in Section 2.1, hydrogen remains in a supercritical fluid state even at high pressure $P^0 = 4$ GPa and ambient temperature $T = 300$ K. For convenience, hereinafter the polycrystalline internal pressure-dependent GTN samples containing the ideal and real hydrogen are referred to as the ideal hydrogen samples and real hydrogen samples, respectively.

Figs. 9 and 10 show the true stress–strain curves and yield strength σ_y at 0.2% offset strain for both the ideal and real hydrogen samples at different values of P^0 and f_v^0, respectively. The yield strengths of these two samples are nearly identical under a given initial state. As the macroscopic tensile strain increases, a notable divergence in flow stress arises between the ideal and real hydrogen samples. This trend aligns with previous theoretical work on the mechanical behavior of porous metals containing gases at constant pressure and ideal gases within voids (Guo et al., 2008). Notably, the stress–strain curves for the real hydrogen samples exhibit a substantially stronger strain-hardening capacity and an extended strain-hardening phase compared to the ideal hydrogen samples. Furthermore, the strain-hardening effect in the real hydrogen sample is closely tied to both the void volume fraction and internal pressure.

For ductile metallic materials, the onset of local necking suggests the initiation of material fracture in experimental study, which is also referred to as the fracture indicator in this work. Based on the Considére stability criterion $\mathrm{d}\sigma_{11}/\mathrm{d}\varepsilon_{11} = \sigma_{11}$, the values of strain and stress, corresponding to the intersection between the true strain–stress curve and work hardening curve, are called as the uniform tensile strain and fracture strength of materials in this work, respectively. In general, this criterion is used to determine the sample performance with unconstrained surface. For these samples, the macroscopic deformation remains almost uniform at necking initiation, consistent with samples constrained by periodic boundary condition. Therefore, in present work, Considére criterion is also adopted to determine the uniform tensile strain and fracture strength of samples in Fig. 8. Fig. 11 shows the uniform tensile strain ε_u and fracture strength σ_f, which characterize the material's ductility and strength, respectively. The simulated macroscopic mechanical performances of the real hydrogen samples surpass those of the ideal hydrogen samples across a broad range of f_v^0 and P^0, with both ductility and strength significantly enhanced in the real hydrogen sample—often several times higher than in the ideal hydrogen sample at high initial void volume fraction ($f_v^0 = 0.03$) and high initial internal pressure ($P^0 = 4$ GPa). In other words, using the ideal gas law EOS to model the internal pressure and density dynamics of hydrogen within voids would considerably overestimate the internal pressure-induced mechanical degradation of porous metallic materials from a trend perspective. Here the fundamental mechanism underlying the nearly identical yield strength as well as the significant distinction in strain-hardening capacity, σ_f, and ε_u presented by two samples can be understood as follows.

Our previous work on the strength–ductility trade-off in nanocrystalline metals has demonstrated that both dislocation accumulation-induced hardening and void damage-induced softening influence a material's macroscopic strain-hardening capacity (Han et al., 2023). In this study, however, we find that dislocation accumulation does not account for the observed differences in strain-hardening capacity between the ideal hydrogen and real hydrogen samples. Fig. 12 plots ratios $(\rho_f^{\text{tol}}/\rho_y^{\text{tol}})^{1/2}$ and σ_f/σ_y at different values of initial internal pressure, where ρ_f^{tol} and ρ_y^{tol} are the volume-weighted total dislocation densities obtained from the numerical simulations at $\sigma_{11} = \sigma_f$ and σ_y, respectively. The ratio $(\rho_f^{\text{tol}}/\rho_y^{\text{tol}})^{1/2}$ is slightly larger than one for all samples. Given that the macroscopic plastic strains remain the same for all samples at 0.2% offset strain, ρ_y^{tol} is considered to be equal, which means that the dislocation accumulation at $\sigma_{11} = \sigma_f$ is almost the same across samples. Based on the Taylor hardening law, which relates macroscopic flow stress to the square root of total dislocation

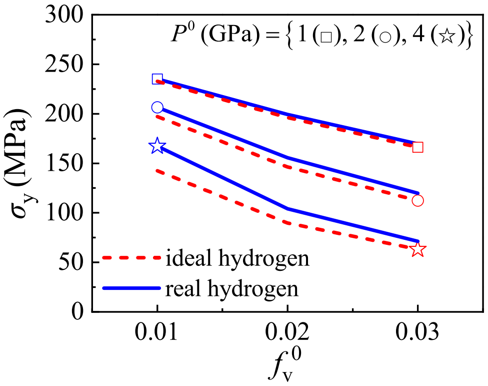

Fig. 10. Tensile yield strength σ_y versus initial void volume fraction f_v^0 at different values of initial internal pressure P^0.

density, one would anticipate that the ratio σ_f/σ_y should approximate one. However, the numerical results show σ_f/σ_y significantly exceeding one for both samples, challenging this assumption. This finding suggests that dislocation accumulation alone does not drive the notable difference in strain-hardening capacity. An additional mechanism must play a central role.

According to Eq. (8), both the void volume fraction and internal pressure affect the macroscopic plastic behavior of materials. To gain more insight into the influence of these two factors on the material strain-hardening capacity, we define dimensionless forms for variables to evaluate their dynamic evolutions. Introducing the dimensionless void volume $\bar{V}_{v,k} = V_{v,k}/V_{v,k}^0$ and dimensionless internal pressure $\bar{P}_k = P_k/P_k^0$ for the k-th integration point, the macroscopic dimensionless void volume and pressure, $\bar{V}_v = \sum_{k=1}^{N_{\mathrm{ipt}}} \bar{V}_{v,k} V_{v,k} / \sum_{k=1}^{N_{\mathrm{ipt}}} V_{v,k}$ and $\bar{P} = \sum_{k=1}^{N_{\mathrm{ipt}}} \bar{P}_k V_{v,k} / \sum_{k=1}^{N_{\mathrm{ipt}}} V_{v,k}$, are defined accordingly, where $V_{v,k}$, $V_{v,k}^0$, P_k, and P_k^0 denote the current and initial void volumes, as well as the current and initial internal pressures of the voids belonging to the k-th integration point, respectively.

Fig. 13 compares the $\bar{P}$–$\bar{V}_v$ curves for the real and ideal hydrogen samples. Due to the straightforward inverse relationship between P and V_m for the ideal hydrogen with EOS $PV_m = RT$, the $\bar{P}$–$\bar{V}_v$ curves of ideal hydrogen samples nearly overlap across a broad range of $\bar{V}_v$. In contrast, for real hydrogen samples with $P^0 = 1$ GPa, 2 GPa, and 4 GPa, the divergence among the $\bar{P}$–$\bar{V}_v$ curves increases with increasing $\bar{V}_v$ at $\bar{V}_v > 1.5$ due to the substantial variability in compressibility with internal pressure (Fig. 1b). As discussed in Section 2.1, real hydrogen resists compression more strongly than ideal hydrogen, resulting in a more rapid decrease in $\bar{P}$ with increasing $\bar{V}_v$ for real hydrogen samples (Fig. 13). Consequently, the void growth rate in real hydrogen samples is slower than in ideal hydrogen samples (Fig. 6). This accelerated reduction in internal pressure in real hydrogen samples alleviates damage faster than void growth can induce it, resulting in a marked rise in macroscopic flow stress. Despite minimal dislocation accumulation within grains during plastic deformation, real hydrogen samples demonstrate significantly stronger strain-hardening and a prolonged strain-hardening phase post-yield compared to ideal hydrogen (Fig. 9). This distinct strain-hardening response accounts for the observed differences in σ_f and ε_u between the two sample types (Fig. 11).

In short words, the compressibility differences between ideal and real hydrogen lead to inaccuracies in estimating the macroscopic mechanical performance of porous metals under internal pressure. Using the ideal gas law EOS, as done in previous studies (Guo et al., 2008; Das et al., 2021), is unsuitable for assessing the residual strength and remaining service life of materials and structures affected by hydrogen embrittlement.

Generally, it may seem intuitive to argue that voids degrade a material's macroscopic mechanical performance, meaning that as the void volume fraction increases, both σ_f and ε_u decrease (as seen, for example, in the ideal hydrogen samples in Fig. 11). However, numerical results from real hydrogen samples reveal an opposite trend, where ε_u actually increases with increasing initial void volume fraction f_v^0 at a certain internal pressure. This strength–ductility trade-off resembles the grain size-dependent competitive relationship seen in nanocrystalline and coarse-grained metals (Li et al., 2020; Sohrabi et al., 2023). The physical mechanism behind this remarkable ductility enhancement with higher initial void volume fraction is explained as follows.

At a certain initial internal pressure, the initial damage extent increases with increasing f_v^0 in the real hydrogen samples. During plastic deformation, void growth quickly alleviates the internal pressure-induced damage, with this damage relief becoming more pronounced at higher f_v^0. For instance, in the case of $P^0 = 4$ GPa (Fig. 9b), samples with larger f_v^0 exhibit a stronger strain-hardening capacity after yielding compared to those with smaller f_v^0, resulting in an upward shift of the strain-hardening rate curve for high f_v^0 samples. Simultaneously, the flow stress decreases as f_v^0 increases. Combining these two aspects, the uniform tensile strain ε_u, defined by the intersection of the strain-hardening rate curve and the strain-stress curve, becomes larger at larger f_v^0. In Appendices C and D, this increasing trend is further verified by adopting a set of parameters for the Benedict-type EOS of helium and a series of values for the void volume fraction in grain boundary, respectively. In addition, at a certain f_v^0, the real hydrogen samples show greater strain-hardening capacity at higher P^0 compared to lower P^0 (Fig. 9). Following the same mechanism, ε_u of the real hydrogen sample increases with P^0 at a given f_v^0 (Fig. 11). A similar trend, where failure tensile strain exhibits an internal pressure-enhanced feature, has been observed in molecular dynamics simulations for both single crystal copper and nano-twinned copper embedded with highly pressurized helium bubbles (Sun et al., 2019; Neogi et al., 2018), verifying the above qualitative numerical results and theoretical analyses.

4.2. Influence of internal pressure on localized necking

Due to the microscopic heterogeneity, random crystallographic orientation, and variable shapes of grains, localized necking is almost inevitable in ductile metals during tensile deformation and can significantly accelerate fracture. Here, we investigate the impact of internal pressure on necking formation using real hydrogen samples with dimensions of 300 μm (length) × 120 μm (width) × 120 μm (height) as shown in Fig. 14, containing $N_G = 375$ grains with an average grain diameter of $d_{\mathrm{ave}} = 29.5$ μm. Unlike the sample constrained by periodic boundary conditions in Fig. 8, a symmetry boundary condition is applied to the cross-sections at $x = y = z = 0$, restricting out-of-plane displacement. As mentioned in Section 4.1, the samples with symmetry boundary condition will present significant deformation localization and local necking at large strains due to random crystallographic orientation.

Fig. 15a presents the true stress–strain curves of the real hydrogen samples shown in Fig. 14, with $f_v^0 = 0.03$. As the initial internal pressure P^0 increases from 0 GPa to 1 GPa and then to 4 GPa, the yield strength and fracture strength decrease from 249.2 MPa and 278 MPa to 167.4 MPa and 225.2 MPa, and then further to 70 MPa and 189.1 MPa, respectively, while the uniform tensile strain correspondingly increases from 0.046 to 0.076 and then to 0.107. Fig. 15b shows the reduction in area $\Phi = 1 - S/S_0$ versus the nominal strain $\varepsilon_{11}^{\mathrm{nom}}$ for the cross-section at $x = 0$, where S and S_0 are the current and initial areas of this cross-section. One can see that the rate of increase in Φ for samples with higher P^0 is slower than that for those with lower P^0, indicating more severe necking in samples with lower P^0 (Fig. 16).

For these real hydrogen samples with symmetry boundary conditions, the enhanced ductility at higher P^0 results from both the

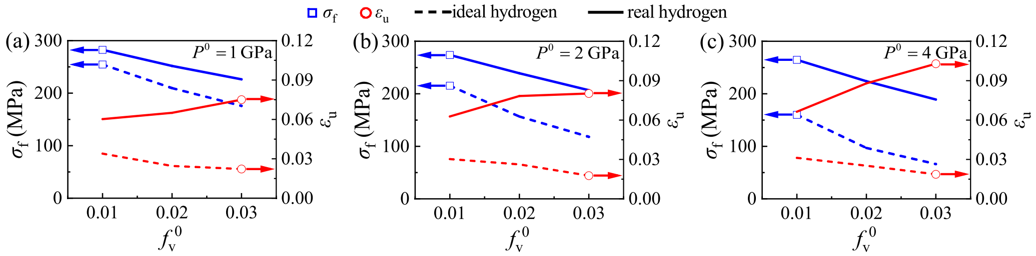

Fig. 11. Qualitative influence of initial void volume fraction f_v^0 on fracture strength σ_f and uniform tensile strain ε_u at initial internal pressure $P^0 = 1$ GPa (a), 2 GPa (b), and 4 GPa (c).

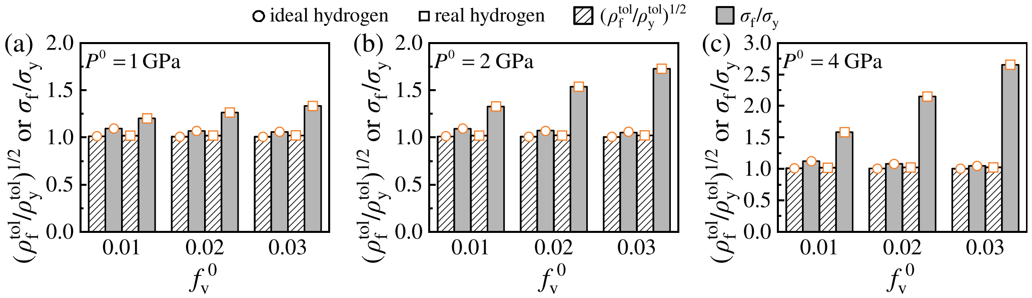

Fig. 12. Ratios $(\rho_f^{tol}/\rho_y^{tol})^{1/2}$ and σ_f/σ_y at initial internal pressures of $P^0 = 1$ GPa (a), 2 GPa (b), and 4 GPa (c).

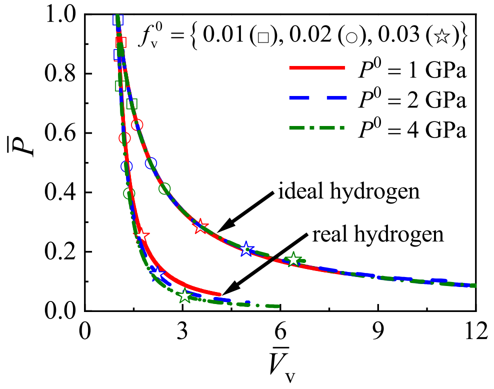

Fig. 13. Dimensionless internal pressure $\bar{P}$ versus dimensionless void volume $\bar{V}_v$ for various initial internal pressure P^0 and initial void volume fraction f_v^0.

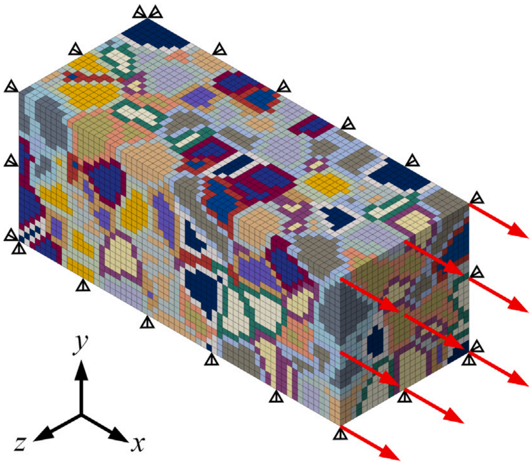

Fig. 14. Polycrystalline model with symmetry boundary conditions. Red arrows, tensile load along x-direction.

increased strain-hardening capacity and the suppression of localized necking, driven by the internal pressure-dependent mechanisms during deformation. In the case with $P^0 = 0$ GPa, strain localization within clustered grains quickly leads to a monotonic decrease in flow stress with increasing ε_{11}^{nom} due to the void growth, rapidly instigating localized necking in a confined region (Fig. 16a). For samples with higher initial internal pressure (e.g., $P^0 = 4$ GPa in Fig. 16c), the internal pressure inside voids rapidly decreases due to void growth. As a result, the macroscopic strength of the material increases markedly with plastic deformation, which in turn hinders further localization by transferring tensile deformation to adjacent grains with lower flow stress. Compared to samples with low P^0, those with higher P^0 involve a greater number of grains in the overall plastic deformation due to sustained load transfer during straining, thereby mitigating strain localization and void growth within specific regions and delaying the onset of localized necking. Our work presents an innovative and in-depth insight for understanding the exceptional enhancement of ductility in single crystal copper with highly pressurized helium nanobubbles, in contrast to the prevailing dislocation-based explanation (Ding et al., 2016).

Our results suggest promising implications for material design strategies. A recent experimental study demonstrated that introducing dispersed nanovoids into pure gold can remarkably enhance both ductility and strength, owing to nanovoid-induced Orowan strengthening and high strain-hardening capacity (J.-J. Chen et al., 2024). Building on the above numerical results and theoretical insights into the effects of voids and their internal pressure on material strength, ductility, and necking behavior, it is reasonable to anticipate that a synergistic improvement in strength and ductility could be achieved in nanovoid-containing pure gold by carefully tuning the internal pressure within the voids. In addition, as mentioned in Section 2.2, the strengthening effect of nanovoid is not taken into account in the present constitutive framework. A physics-based constitutive model incorporating nanovoid strengthening effect is highly desired in future work.

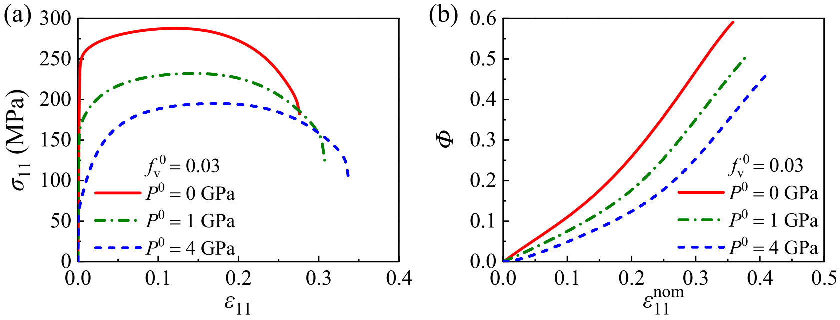

Fig. 15. (a) True stress–strain curves for the polycrystalline samples in Fig. 14 with $f_v^0 = 0.03$ at different values of P^0. (b) Cross-sectional area reduction Φ at $x = 0$ versus nominal strain ε_{11}^{nom}.

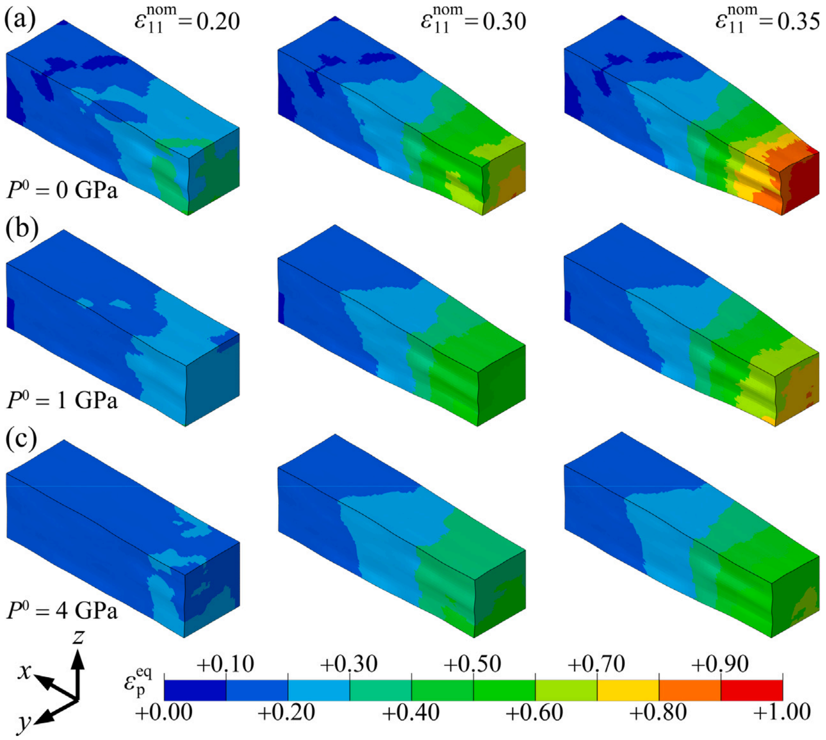

Fig. 16. Contour plots of equivalent plastic strain ε_p^{eq} for samples with initial internal pressure $P^0 = 0$ GPa (a), 1 GPa (b), and 4 GPa (c) at different values of the nominal strain ε_{11}^{nom}.

5. Conclusions

A physics-based crystal plasticity model for high-internal-pressure porous metals has been developed, integrating the Benedict equation of state (EOS) for real hydrogen into the internal pressure-dependent Gurson–Tvergaard–Needleman potential. This model qualitatively elucidates the effects of EOS choice, initial void volume fraction, and initial internal pressure on macroscopic properties — yield strength, fracture strength, uniform tensile strain — and microstructural evolution, including void growth, internal pressure variation, and necking formation, thus providing insights into the mechanisms underlying hydrogen embrittlement in metals. Based on the crystal plasticity finite element method, qualitative key findings are as follows.

Our numerical simulations demonstrate that for porous metals under internal pressure, applying the ideal gas EOS, from a trend perspective, substantially underestimates strength and ductility. The Benedict-type EOS is essential to assess residual strength and service life in hydrogen-embrittled materials. Meanwhile, for hydrogen that follows the Benedict-type EOS, porous metals with a high initial void volume fraction show greater strain-hardening capacity and an extended strain-hardening phase, which mitigates damage more effectively than metals with a low initial void fraction. Incorporating the decrease in macroscopic flow stress, the uniform tensile strain of metals is enlarged at large initial volume fraction of voids. This mechanism also explains the enhanced ductility with increasing initial void internal pressure at a given void volume fraction. In addition, a reduction in the internal pressure of voids with the Benedict-type EOS enhances the macroscopic strain-hardening capacity of materials, mitigates strain localization, and delays the formation of localized necking. Strategically adjusting internal void pressure could thus improve strength–ductility synergy in metallic materials with nanovoids.

While developed for hydrogen-filled porous metals, this model provides a versatile framework that could be extended to study void swelling and helium embrittlement in irradiated metallic materials. It

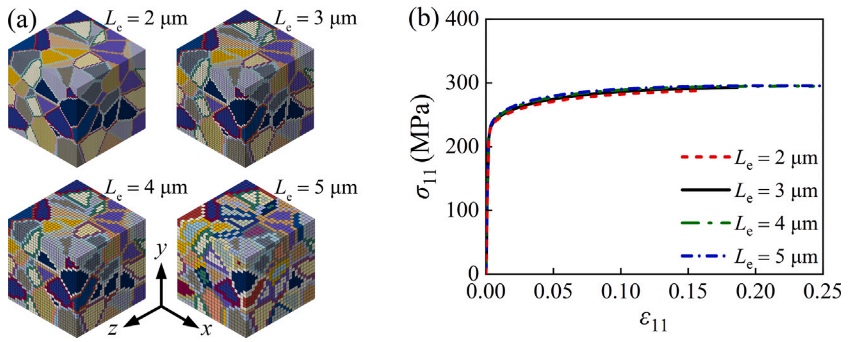

Fig. B.1. (a) Finite element models with different mesh resolutions, and (b) corresponding stress–strain responses under uniaxial tension along x-direction for the real hydrogen sample with $f_v^0 = 0.01$ and $P = 1$ GPa. Due to the high computational cost associated with nonlinear implicit analysis, the simulation with the 2 μm mesh was performed up to $\varepsilon_{11} = 0.072$, covering both the elastic–plastic transition and strain-hardening regimes.

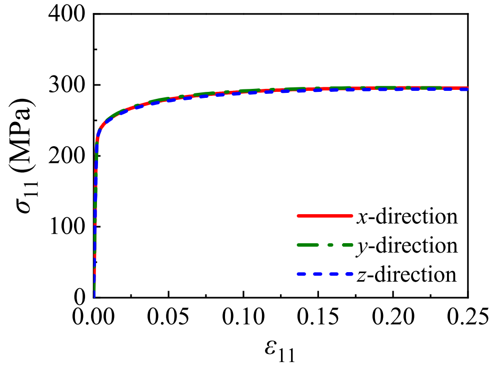

Fig. B.2. The stress–strain curves of real hydrogen sample with element size $L_e = 5$ μm in Fig. B.1a under different loading directions.

is important to note that hydrogen diffusion in the metallic matrix, mass exchange between the matrix and hydrogen bubbles, nanovoid strengthening effect, and hydrogen-regulated dislocation evolution significantly influence hydrogen embrittlement, particularly in steels and other metals. A more comprehensive theoretical and numerical investigation incorporating these effects is warranted in future studies.

CRediT authorship contribution statement

Quanfeng Han: Writing – review & editing, Writing – original draft, Software, Methodology, Investigation, Funding acquisition, Formal analysis, Conceptualization. **Jingli Li:** Investigation, Formal analysis. **Hui Wang:** Investigation, Formal analysis. **Yizhe Chen:** Writing – review & editing, Supervision, Methodology, Investigation, Funding acquisition, Formal analysis, Conceptualization. **Xin Yi:** Writing – review & editing, Supervision, Methodology, Investigation, Formal analysis, Conceptualization. **Lin Hua:** Writing – review & editing, Supervision, Investigation, Formal analysis.

Declaration of competing interest

The authors declare that they have no known competing financial interests or personal relationships that could have appeared to influence the work reported in this paper.

Acknowledgments

This work was supported by the National Natural Science Foundation of China (NSFC) (Grant Nos. 12402129, 52422510, and 12588201) and the Natural Science Foundation of Hubei Province, China (Grant No. 2025AFD124). Computational resources provided by the High-Performance Computing Platform of Wuhan University of Technology and Peking University are acknowledged.

Appendix A. Determination for internal pressure of voids

As mentioned in Section 2.1, the internal pressure of hydrogen bubbles varies with the evolution of void volume. This Appendix details the derivations for calculating the pressure of both real and ideal hydrogen within these bubbles.

Assuming no mass exchange of hydrogen between the dense matrix and the bubble, the following mass conservation equation for hydrogen within voids at a given material point holds

$$\rho_h^0 f_v^0 V_{ipt}^0 = \rho_h^j f_v^j V_{ipt}^j, \tag{A.1}$$

where ρ_h, f_v, and V_{ipt} represent the density of hydrogen, void volume fraction, and integration point volume in the finite element simulations, respectively. The superscripts 0 and j refer to the initial state and the state at the end of the j-th time increment, respectively. The ABAQUS software's UVARM subroutine enables the extraction of V_{ipt}^0 and V_{ipt}^j values.

For the real hydrogen, recalling Eq. (1) and introducing $V_m = M_h/\rho_h$ with M_h as the molar mass of hydrogen, Eq. (A.1) becomes

$$\rho_h^0 f_v^0 V_{ipt}^0 = \frac{M_h}{\sum_{m=1}^{3} \sum_{n=-2}^{2} A_{n,m} (T^j)^{n/2} (P^j)^{-m/3}} f_v^j V_{ipt}^j, \tag{A.2}$$

where P^j and T^j are the current internal pressure and absolute temperature of the hydrogen within the voids. Given the extremely small macroscopic strain rate of 10^{-4}/s in the simulation and the adequate heat exchange among the environment, metallic matrix, and hydrogen bubbles during deformation, the heat generated by plastic deformation is expected to have a negligible effect on the temperature of the dense matrix and bubbles. Therefore, we assume a constant temperature for the hydrogen inside the voids. Then, the internal pressure P of the real hydrogen can be determined iteratively from Eq. (A.2) in the numerical calculations.

For the ideal hydrogen, from $PV_m = RT$ and $V_m = M_h/\rho_h$, one has $\rho_h^0 f_v^0 V_{ipt}^0 = [M_h P^j/(RT^j)] f_v^j V_{ipt}^j$. Then the explicit solution for the internal pressure of the ideal hydrogen at the end of the j-th time increment is

$$P^j = \frac{\rho_h^0 f_v^0 V_{ipt}^0 RT^j}{M_h f_v^j V_{ipt}^j}. \tag{A.3}$$

Appendix B. Sensitivity to loading direction and mesh resolution of polycrystalline model

Taking the real hydrogen sample with $f_v^0 = 0.01$ and $P = 1$ GPa as an example, this Appendix explores the sensitivity of macroscopic

Table C.1
Dimensionless parameters of the Benedict-type EOS for real helium (Mills et al., 1980).

n	$A_{n,1}$	$A_{n,2}$	$A_{n,3}$
−2	0	0	189.84
−1	−7.2645	0	−19.641
0	22.575	−12.483	1.0596
1	0	0	0
2	0.0064655	−0.024549	0.10604

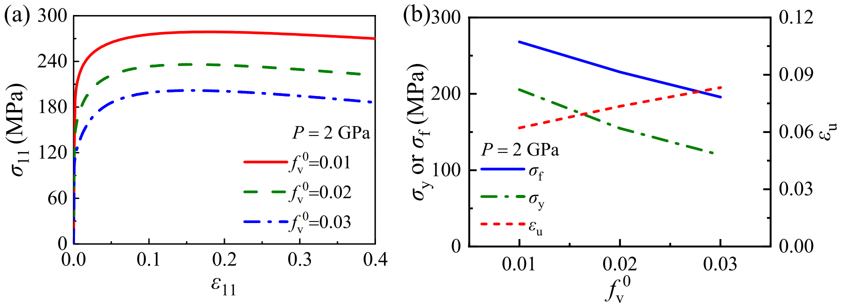

Fig. C.1. (a) True stress–strain curves of real helium samples with different initial void volume fractions at $P = 2$ GPa and $T = 295.15$ K. (b) Yield strength σ_y, fracture strength σ_f, and uniform tensile strain ε_u as functions of initial void volume fraction f_v^0.

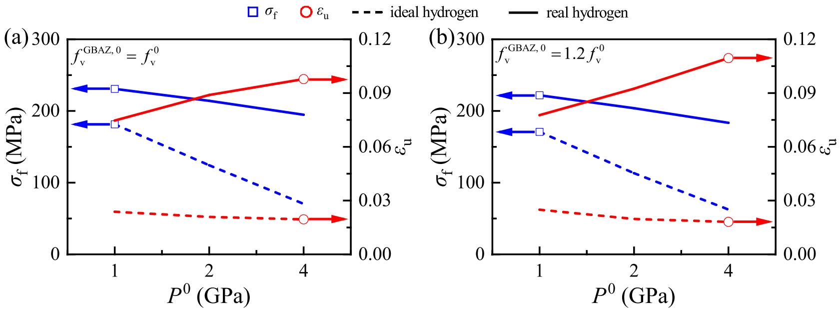

Fig. D.1. Qualitative influence of initial internal pressure P^0 on fracture strength σ_f and uniform tensile strain ε_u at void volume fraction in grain boundary zone $f_v^{GBAZ,0} = f_v^0$ (a) and $1.2 f_v^0$ (b) with $f_v^0 = 0.03$.

mechanical response to the mesh resolution and loading direction for polycrystalline material to ensure the reliability of numerical results.

Fig. B.1a shows the finite element models which share with the model in Fig. 8 the same seed points of Voronoi diagram but have different mesh resolutions by setting element size L_e = 2 μm, 3 μm, 4 μm, and 5 μm. The simulated uniaxial tensile curves with uniaxial loading along x-direction in Fig. B.1b indicate that mesh size has infinitesimal influence on the macroscopic flow stress of material with decreasing element size below 5 μm, although the regions within grain boundary affected zone vary with mesh size. Therefore, in view of the convergence of numerical results and the computational efficiency, the finite element model with L_e = 5 μm is employed in this work.

Fig. B.2 compares the stress–strain curves of real hydrogen sample with element size 5 μm in Fig. B.1a under different loading directions. One can see that these curves almost overlap, consistent with the error estimation analyzed in Section 4.1. It demonstrates that the microscopic heterogeneity of grain have little effect on the macroscopic flow stress for ploycrystalline model containing 150 grains.

Appendix C. Verification for increase in uniform tensile strain by helium bubble

Using the parameters of Benedict-type EOS for real helium in Table C.1, this Appendix further verifies the increase of uniform tensile strain with increasing initial volume fraction. As shown in Fig. C.1, the flow stress of polycrystalline samples decreases with increasing initial void volume fraction f_v^0 at P = 2 GPa and T = 295.15 K, leading to the reductions in yield strength σ_y and fracture strength σ_f. However, the uniform tensile strain ε_u remains showing a rising trend, further validating the damage relief-induced ductility increase as discussed in Section 4.1.

Appendix D. Verification for different trends of strength and ductility in ideal and real hydrogen samples

By taking the void volume fraction in grain boundary zone $f_v^{GBAZ,0} = f_v^0$ and $1.2 f_v^0$, this appendix further verifies the different trends of strength and ductility for the ideal and real gas samples. Fig. D.1 demonstrates that the ideal hydrogen samples always present lower strength and ductility than the real hydrogen samples, accompanied by decreasing trends with increasing P^0. In contrast, the uniform tensile strain ε_u presents significant increase for the real hydrogen samples, despite a slight decrease in the fracture strength σ_f. These numerical results further validate the enhanced ductility with increasing initial void internal pressure in Section 4.1.

Data availability

Data will be made available on request.

References

Chen, Y.-S., Huang, C., Liu, P.-Y., Yen, H.-W., Niu, R., Burr, P., Moore, K., Martínez-Pañeda, E., Atrens, A., Cairney, J., 2024. Hydrogen trapping and embrittlement in metals – A review. Int. J. Hydrog. Energy 136, 789–821.

Chen, Y.-S., Lu, H., Liang, J., Rosenthal, A., Liu, H., Sneddon, G., McCarroll, I., Zhao, Z., Li, W., Guo, A., Cairney, J., 2020. Observation of hydrogen trapping at dislocations, grain boundaries, and precipitates. Science 367, 171–175.

Chen, Y., Ma, X., Han, Q., Yang, D., Xiao, Y., Wang, H., Hua, L., 2025. Crystallographic texture and grain refinement regulated low-cycle fatigue performance of 6061-T6 aluminum alloy. Eng. Failure Anal. 186, 110486.

Chen, J.-J., Xie, H., Liu, L.-Z., Guan, H., You, Z., Zou, L., Jin, H.-J., 2024. Strengthening gold with dispersed nanovoids. Science 385, 629–633.

Condon, J., Schober, T., 1993. Hydrogen bubbles in metals. J. Nucl. Mater. 207, 1–24.

Das, S., Song, D., Castañeda, P., 2021. Macroscopic response and microstructure evolution in viscoplastic polycrystals with pressurized pores. Int. J. Fract. 230, 43–70.

Diatschenko, V., Wu, C.W., Liebenberg, D.H., Young, D.A., Ross, M., Mills, R.L., 1985. Melting curves of molecular hydrogen and molecular deuterium under high pressures between 20 and 373 K. Phys. Rev. B 32, 381–389.

Ding, M.-S., Du, J.-P., Wan, L., Ogata, S., Tian, L., Ma, E., Han, W.-Z., Li, J., Shan, Z.-W., 2016. Radiation-induced helium nanobubbles enhance ductility in submicron-sized single-crystalline copper. Nano Lett. 16, 4118–4124.

Ebling, F., Bratsch, P., Wagner, S., Pundt, A., Preußner, J., Oesterlin, H., Wackermann, K., Michler, T., 2025. Assessing hydrogen embrittlement of alloy 718: Hollow and conventional tensile tests. Eng. Fract. Mech. 319, 111028.

Fu, J., Wu, L., Yu, L., Sui, H., Zhang, J., Duan, H., Mao, S., 2024. Modelling the effects of void swelling and spatial heterogeneity on the fracture of metallic materials by crystal plasticity. Proc. R. Soc. A 480, 20240028.

Geng, W., Wan, L., Du, J.-P., Ishii, A., Ishikawa, N., Kimizuka, H., Ogata, S., 2017. Hydrogen bubble nucleation in α-iron. Scr. Mater. 134, 105–109.

Guo, T., Faleskog, J., Shih, C., 2008. Continuum modeling of a porous solid with pressure-sensitive dilatant matrix. J. Mech. Phys. Solids 56, 2188–2212.

Gurson, A., 1977. Continuum theory of ductile rupture by void nucleation and growth: Part I–Yield criteria and flow rules for porous ductile media. J. Eng. Mater. Technol. 99, 2–15.

Halilović, A.E., Faleskog, J., Efsing, P., 2023. An experimental fracture mechanics study of the combined effect of hydrogen embrittlement and loss of constraint. Eng. Fract. Mech. 289, 109460.

Han, X., Besson, J., Forest, S., Tanguy, B., Bugat, S., 2013. A yield function for single crystals containing voids. Int. J. Solids Struct. 50, 2115–2131.

Han, Q., Li, J., Yi, X., 2023. Overcoming strength–ductility trade-off of nanocrystalline metals by engineering grain boundary, texture, and gradient microstructure. J. Mech. Phys. Solids 173, 105200.

Hemmes, H., Driessen, A., Griessen, R., 1986. Thermodynamic properties of hydrogen at pressures up to 1 Mbar and temperatures between 100 and 1000 K. J. Phys. C: Solid State Phys. 19, 3571–3585.

Hill, R., 1952. The elastic behaviour of a crystalline aggregate. Proc. Phys. Soc. A 65, 349–354.

Hou, J., Kong, X.-S., Wu, X., Song, J., Liu, C., 2019. Predictive model of hydrogen trapping and bubbling in nanovoids in bcc metals. Nat. Mater. 18, 833–839.

Hu, J., Xu, B., Yu, C., Kang, G., 2024. Plastic deformation of magnesium single crystal: a crystal plasticity coupled twinning phase field simulation. Acta Mech. Sin. 40, 423337.

Huang, L., Chen, D., Xie, D., Li, S., Zhang, Y., Zhu, T., Raabe, D., Ma, E., Li, J., Shan, Z., 2023. Quantitative tests revealing hydrogen-enhanced dislocation motion in α-iron. Nat. Mater. 22, 710–716.

Hutchinson, J., 1976. Bounds and self-consistent estimates for creep of polycrystalline materials. Proc. R. Soc. A 348, 101–127.

Johnson, W., 1875. On some remarkable changes produced in iron and steel by the action of hydrogen and acids. Proc. R. Soc. Lond. 23, 168–179.

Kim, J., Lee, M.-G., Kang, J.-H., Oh, C.-S., Barlat, F., 2017. Crystal plasticity finite element analysis of ferritic stainless steel for sheet formability prediction. Int. J. Plast. 93, 26–45.

Kourougianni, F., Arsalis, A., Olympios, A., Yiasoumas, G., Konstantinou, C., Papanastasiou, P., Georghiou, G., 2024. A comprehensive review of green hydrogen energy systems. Renew. Energy 231, 120911.

Li, X., Lu, L., Li, J., Zhang, X., Gao, H., 2020. Mechanical properties and deformation mechanisms of gradient nanostructured metals and alloys. Nat. Rev. Mater. 5, 706–723.

Lindblom, D., Dahlberg, C.F.O., 2025. A strain gradient plasticity model to investigate diffusion and dynamic segregation of hydrogen. Eur. J. Mech./A Solids 111, 105527.

Liu, H., Lu, L., Luo, H., Deng, J., Li, G., Ning, H., Fan, Y., Huang, C., Lan, Z., Zhou, W., Guo, J., Wang, X., 2024. Hybrid of bulk NbC and layered Nb_4C_3 MXene for tailoring the hydrogen storage kinetics and reversibility of Li–Mg–B–H composite: An experimental and theoretical study. J. Mater. Sci. Technol. 194, 225–235.

Lopez-Cazalilla, A., Djurabekova, F., Granberg, F., Mizohata, K., Perez-Fontenla, A., Calatroni, S., Wuensch, W., 2022. Punching of arbitrary face prismatic loops from hydrogen nanobubbles in copper. Acta Mater. 225, 117554.

Lopez-Cazalilla, A., Serafim, C., Kimari, J., Ghaemi, M., Perez-Fontenla, A., Calatroni, S., Grudiev, A., Wuensch, W., Djurabekova, F., 2024. Effect of surface orientation on blistering of copper under high fluence keV hydrogen ion irradiation. Acta Mater. 266, 119699.

Magri, M., 2025. A diffuse interface model for electro-chemo-mechanical systems. Eur. J. Mech./A Solids 109, 105470.

Martinsson, Å., Sandström, R., 2012. Hydrogen depth profile in phosphorus-doped, oxygen-free copper after cathodic charging. J. Mater. Sci. 47, 6768–6776.

Matsuishi, K., Gregoryanz, E., Mao, H., Hemley, R., 2002. Brillouin and Raman scattering of fluid and solid hydrogen at high pressures and temperatures. J. Phys.: Condens. Matter 14, 10631–10636.

Mills, R., Liebenberg, D., Bronson, J., 1980. Equation of state and melting properties of ^{4}He from measurements to 20 kbar. Phys. Rev. B 21, 5137–5148.

Miura, T., Fujii, K., Fukuya, K., 2015. Micro-mechanical investigation for effects of helium on grain boundary fracture of austenitic stainless steel. J. Nucl. Mater. 457, 279–290.

Neogi, A., Askari, H., Abdolrahim, N., 2018. Atomistic simulations of the strengthening effect of high-density bubble formation in helium irradiated single crystalline copper. Materialia 1, 139–149.

Niu, R., Li, H., Liu, P.-Y., Burr, P., Feng, Y., Yen, H.-W., Huang, C., Sun, Y.-H., Ma, M., Guo, A., Lu, H., Chen, Y.-S., Cairney, J.M., 2024. Hydrogen-enhanced deformation in pearlite. Acta Mater. 281, 120327.

Nygårds, M., 2003. Number of grains necessary to homogenize elastic materials with cubic symmetry. Mech. Mater. 35, 1049–1057.

Park, J., Shin, G., Kim, H., Kim, K., Yoon, S., Sohn, S., Lee, M.-G., 2024. A continuum scale chemo-mechanical model for multi-trap hydrogen transport in deformed polycrystalline metals. Int. J. Plast. 173, 103892.

Peters, T., Carvalho, P., Stange, M., Bredesen, R., 2020. Formation of hydrogen bubbles in Pd-Ag membranes during H_2 permeation. Int. J. Hydrog. Energy 45, 7488–7496.

Pinto, D.L., Tuhami, A.E.O., Osipov, N., Madi, Y., Besson, J., 2024. Simulation of hydrogen embrittlement of steel using mixed nonlocal finite elements. Eur. J. Mech./A Solids 104, 105116.

Prewitz, M., Bardenhagen, A., Beck, R., 2020. Hydrogen as the fuel of the future in aircrafts – Challenges and opportunities. Int. J. Hydrog. Energy 45, 25378–25385.

Robertson, I., Sofronis, P., Nagao, A., Martin, M., Wang, S., Gross, D., Nygren, K., 2015. Hydrogen embrittlement understood. Metall. Mater. Trans. B 46, 1085–1103.

Sahiluoma, P., Yagodzinskyy, Y., Bossuyt, S., Hänninen, H., 2023. Hydrogen-induced micro-void formation in copper used for spent nuclear fuel disposal canisters. J. Nucl. Mater. 574, 154177.

Sohrabi, M., Mirzadeh, H., Sadeghpour, S., Mahmudi, R., 2023. Grain size dependent mechanical behavior and TRIP effect in a metastable austenitic stainless steel. Int. J. Plast. 160, 103502.

Sun, J., Li, Q., Tang, H., Zhang, H., Ye, H., Zheng, Y., 2019. Helium implantation effects on the tensile response of nano-twinned copper. J. Nucl. Mater. 541, 152426.

Takeuchi, T., 1975. Work hardening of copper single crystals with multiple glide orientations. Trans. Jpn. Inst. Met. 16, 629–640.

Tan, A., Li, Z., Zhao, Y., Ramamurty, U., Gao, H., 2024. Modeling the improved hydrogen embrittlement tolerance of twin boundaries in face-centered cubic complex concentrated alloys. J. Mech. Phys. Solids 188, 105657.

Varshni, Y., 1970. Temperature dependence of the elastic constants. Phys. Rev. B 2, 3952–3958.

Walgraef, D., Ghoniem, N., 1990. Patterns, Defects and Materials Instability. Kluwer Academic Publishers, Dordrecht, Netherlands.

Wu, C., Li, H., 2025. Towards accurate prediction of thermodynamic properties of hydrogen over supercritical conditions using volume-translated cubic equations of state. Geoenergy Sci. Eng. 252, 213924.

Xiao, X., Song, D., Chu, H., Xue, J., Duan, H., 2015. Mechanical properties for irradiated face-centred cubic nanocrystalline metals. Proc. R. Soc. A 471, 20140832.

Xing, X., Gou, J., Li, F., Zhang, Y., Cheng, J., Wang, Y., Liu, J., Cui, G., Li, Z., Zhang, P., Luo, X., Wang, B., 2021. Hydrogen effect on the intergranular failure in polycrystal α-iron with different crystal sizes. Int. J. Hydrog. Energy 46, 36528–36538.

Xing, X., Li, F., Liu, J., Cui, G., Li, Z., Cheng, Y., 2024. Molecular dynamics modeling of hydrogen-induced plastic deformation and cracking of α-iron. J. Mater. Sci. Technol. 176, 119–131.

Xu, Z., Liu, S., Zhu, Y., Shi, R., Gao, K., Pang, X., 2025. In situ investigation of hydrogen embrittlement induced by δ phase in selective laser-melted GH4169 superalloy. J. Mater. Sci. Technol. 211, 145–158.

Yan, L., Yin, Z., Yue, M., Yan, W., Deng, J., Li, H., 2025. Regulating hydrogen adsorption via built-in electric field-driven charge transfer at the heterointerface for enhanced alkaline/seawater hydrogen evolution. J. Mater. Sci. Technol. 236, 215–224.

Yu, L., Sui, H., Liu, W., Chen, L., Liu, Y., Duan, H., 2020. A yield criterion for porous crystalline materials with inner pressure. Int. J. Solids Struct. 202, 511–520.

Yuan, S., Zhu, Y., Huang, M., Zhao, L., Liang, S., Li, Z., 2023. A coupled diffusional-mechanical model accounting for hydrogen enhancements of strain-induced dislocations and vacancies. Mech. Mater. 186, 104781.

Zepeda-Ruiz, L., Stukowski, A., Oppelstrup, T., Bertin, N., Barton, N., Freitas, R., Bulatov, V., 2021. Atomistic insights into metal hardening. Nat. Mater. 20, 315–320.

Zhang, J., Sheng, Y., Yang, H., Ma, W., Jiang, X., 2023. Crystal crack dislocation model and micro-crack nucleation criterion in the hydrogen environment. Eur. J. Mech./A Solids 98, 104899.

Zhao, H., Zheng, X., Yang, S., Yang, X., Li, W., 2024. Direct FE^2 multiscale simulation of hydrogen diffusion in zircaloy cladding. Acta Mech. Sin. 40, 124270.

Zhao, Q., Zhu, Q., Zhang, Z., Yin, B., Gao, H., Zhou, H., 2024. A machine learning-based framework for mapping hydrogen at the atomic scale. Proc. Natl. Acad. Sci. USA 121, e2410968121.